Colloidal systems in three-dimensional microchannels: lattice control via channel width and external force

Nadine Schwierz, Peter Nielaba

Angaben zur Veröffentlichung / Publication details:

Schwierz, Nadine, and Peter Nielaba. 2010. "Colloidal systems in three-dimensional microchannels: lattice control via channel width and external force." *Physical Review E* 82 (3): 031401. https://doi.org/10.1103/physreve.82.031401.

Colloidal systems in three-dimensional microchannels: Lattice control via channel width and external force

Nadine Schwierz[1] and Peter Nielaba[2]
[1]*Physik Department, Technische Universität München, 85748 Garching, Germany*
[2]*University of Konstanz, 78457 Konstanz, Germany*
(Received 9 July 2010; published 3 September 2010)

The structural behavior of hard spheres interacting with repulsive (screened Coulomb) interaction in narrow constrictions is investigated using Brownian dynamics simulations. The system of particles adapts to the confining potential and the interaction energies by a self-consistent arrangement of the particles. It results in the formation of planes throughout the three-dimensional channel. The presence of hard walls leads to structural deviations from the unbounded (infinite) crystal. The arrangement of the particles is perturbed by diffusion and an external driving force leading to a density gradient along the channel. The particles accommodate to the density gradient by reducing the number of planes if it is energetically favorable. This reduction in the number of planes is analogous to the reduction in the number of layers in two-dimensional systems. The influence of a self-organized order within the system is reflected in the velocity of the particles and their diffusive behavior.

DOI: 10.1103/PhysRevE.82.031401 PACS number(s): 82.70.Dd, 05.45.−a, 83.10.Rs

I. INTRODUCTION

While the equilibrium properties of colloidal systems in bulk are extensively studied and understood by now, important questions concerning colloids in confined geometries or in nonequilibrium are still open [1]. Such systems can serve as model systems for complex processes such as the dynamic behavior of lattice defects, the transport of interaction particles through narrow constrictions, which is important in biological systems like ion channels [2], or nonequilibrium transport and mixing phenomena on the micrometer scale in the context of microfluidics and "lab-on-a-chip" devices [3]. The advantage of using colloidal systems as model systems is that they are experimentally easily accessible and can help one to understand the underlying physics governing complex processes.

The formation of lanes along the direction of motion is a prominent feature and occurs in various systems with interacting entities such as pedestrians in a pedestrian zone [4] or ants following a trail to food places. For colloidal particles this formation of layers has been studied both in two-dimensional (2D) [5–7] and in three-dimensional (3D) [8–10] systems. So far there are no experimental studies for such systems. However, first hints for a lane formation transition occur in oppositely charged colloids driven in opposite directions by an electric field [11] or in binary complex plasmas under microgravity conditions [12]. The transport behavior of superparamagnetic colloids confined in 2D microchannels has been investigated both experimentally and by Brownian dynamics simulations [13,14]. Such driven diffusive systems serve as model systems for the theoretical studies of nonequilibrium behavior [15]. Moreover, such systems correspond to the classical case of a quantum point contact in mesoscopic electronics [16] or in metallic single point contacts [17,18] with transport occurring due to quantization effects in electronic channels. Due to a confinement, a classical 2D system forms a layered structure in equilibrium [19,20] and the change in the number of layers due to the geometry of the confinement has been predicted using Langevin dynamics simulations [21]. The layers in the macroscopic transport can be seen as analogous to quantum channels since in both transport occurs due to the interaction of the particles with the confining potential.

In this work we investigate the structural behavior of particles interacting via a Yukawa hard-core (YHC) potential in 2D and 3D microchannels. Particles interacting via a YHC potential serve as a model for charge stabilized suspensions consisting of colloidal particles suspended in a polar solvent with coions and counterions and occur in various physical systems including elementary particles or charged dust grains in a plasma environment. The phase diagram of YHC particles has been studied extensively in experiments [22–25] as well as by computer simulations [26,27] and is similar to the phase diagram of hard spheres [25]. It has been shown that confinement of 2D system of interacting particles in narrow channels leads to the formation of layers, in order to conform to the boundaries set by the hard walls [19,28,29]. The number and stability of these layers change as the density, the interaction potential of the particles, or the boundary conditions are varied. In this paper we address the question of whether analogous structural changes as observed in 2D systems occur in 3D systems as well. Moreover, we investigate the reduction in the number of planes when the particles are subject to a driven motion along the channel.

The organization of the paper is as follows. In Sec. II we provide the simulation details used in the present study. In Sec. III we discuss the structural properties of the 2D microchannels focusing on the reduction in the number of layers due to the influence of an external driving force. We analyze the influence of a confinement on the structural properties in 3D channels in equilibrium and finally investigate the nonequilibrium transport behavior. The results of this study are summarized in Sec. IV.

II. MODEL AND METHODS

A. Interaction potential

The system consists of purely repulsive particles interacting via the YHC potential

$$\frac{\mathcal{V}_{ij}(r_{ij})}{k_BT} = \begin{cases} \infty, & r_{ij} < \sigma \\ U\dfrac{\exp\{-\kappa\sigma(r_{ij}/\sigma - 1)\}}{r_{ij}/\sigma}, & \sigma \le r_{ij} \le R_{\text{cut}} \\ 0, & r_{ij} > R_{\text{cut}}, \end{cases} \quad (1)$$

where r_{ij} is the distance between the centers of the particles i and j, U is the value of the pair potential at contact, κ is the inverse Debye screening length, $\sigma=4.55$ μm is the hard-core diameter of the colloids, and R_{cut} is a density-dependent cutoff of the interaction potential. Note, that with the help of the Derjaguin-Landau-Verwey-Overbeek (DLVO) theory [30,31] the contact value U can be written as

$$U = \frac{Z^2}{(1+\kappa\sigma/2)^2}\frac{\lambda_B}{\sigma}, \quad (2)$$

where $\lambda_B = e^2/4\pi\epsilon_0\epsilon_S k_B T$ is the Bjerrum length with the solvent dielectric constant ϵ_S and the charge of the colloids Z. The total potential energy of N particles is given by the sum over all pair interactions,

$$\mathcal{U}(\mathbf{r}_1, \ldots, \mathbf{r}_N) = \sum_{i<j}^{N} \mathcal{V}(r_{ij}). \quad (3)$$

B. Brownian dynamics simulations

The Brownian dynamics Simulations are based on the overdamped Langevin equation, neglecting hydrodynamic interactions as well as short-time momentum relaxation of the particles. The colloidal trajectories are approximated by the stochastic position Langevin equation with the friction constant ξ,

$$\xi\frac{d\mathbf{r}_i(t)}{dt} = -\nabla_{\mathbf{r}_i}\sum_{i\neq j}\mathcal{V}_{ij}(r_{ij}) + \mathbf{F}_i^{(\text{ext})} + \tilde{\mathbf{F}}_i(t). \quad (4)$$

The right-hand side includes the particle interaction as a sum over all forces acting on each particle, with the constant driving force $\mathbf{F}_i^{(\text{ext})}$ and the random forces $\tilde{\mathbf{F}}_i$ describing the random collisions of the solvent molecules with the ith colloidal particle. The latter is in the simulation given by a random number with zero mean $\langle\tilde{\mathbf{F}}_i(t)\rangle=0$ and variance $\langle\tilde{\mathbf{F}}_{i\alpha}(t)\tilde{\mathbf{F}}_{j\beta}(0)\rangle = 2k_BT\delta(t)\delta_{ij}\delta_{\alpha\beta}$, where k_B denotes the Boltzmann constant, T is the temperature, and the subscripts α and β are the Cartesian components. Equation (4) is integrated forward in time using a finite time step Δt and the technique by Ermak [32]. A density-dependent cutoff is used for the interaction potential which has a value of $R_{\text{cut}}=6.5R$, where $R=(2\rho/\sqrt{3})^{-1/2}$ in the 2D systems and $R=\rho^{-1/3}$ in the 3D systems. The 2D channels have a length of $L_x=800\sigma$ and a width of $L_y=10\sigma$ containing 3200 particles corresponding to a density of $\rho=0.4\sigma^{-2}$. The 3D channels have a quadratic square section of $L_y=L_z=5\sigma$ and a length of $L_x=1000\sigma$ containing about 10 000 particles with a fixed particle density of $\rho=0.4\sigma^{-3}$. The particles are confined within the channels by ideal hard walls. The equilibrium configuration in a closed channel is calculated starting from a random configuration and applying hard wall boundary conditions in all directions. The systems are typically equilibrated over 2×10^5 time steps. The time step $\Delta t=7.5\times10^{-5}t_B$ is used where $t_B=\xi\sigma^2/k_BT$ is the time a particle needs in equilibrium to diffuse its own diameter σ. The friction constant ξ is chosen to be $\xi=3\pi\eta\sigma=4.288\times10^{-8}$ N s/m, where $\eta=0.001$ Pa s is the shear viscosity of water. The simulations are done at a constant temperature of $T=295$ K. To study the influence of an external force, a constant driving force of $F_{\text{ext}}=2.603\times10^{-15}$ N is applied in the longitudinal direction. The channel end is then realized by an open boundary condition. To keep the number density in the channel fixed a new particle is inserted within the first 10% of the channel at a random position avoiding overlaps every time a particle leaves the open end of the channel acting as a particle reservoir. For the simulation of the unconfined system a cubic simulation box with an extension of 20σ and periodic boundary conditions in x, y, and z directions is used containing 3200 particles corresponding to a density of $\rho=0.4\sigma^{-3}$.

C. Layer order parameter

The point of an increase or reduction in the number of layers in a 2D microchannel can be well localized by an appropriate local order parameter. Therefore, the channel of width L_y is divided into several bins in the x direction. Every bin contains n_{bin} particles. An order parameter in dependence of the number of layers can be defined as [13]

$$\Psi_{\text{layer}}(n_l) = \left|\frac{1}{n_{\text{bin}}}\sum_{j=1}^{n_{\text{bin}}}\exp\{i[2\pi(n_l-1)/L_y]y_j\}\right|. \quad (5)$$

This layer order parameter is unity if the particles are distributed equidistantly in n_l layers over the width of the channel. Analogously, in a 3D channel the increase or reduction in the number of planes can be localized by dividing the channel in the x direction into several bins according to the mean particle separation in the x direction. For each bin with square section $L_y\times L_z$ the order parameter of the number of planes n_P is defined as

$$\Psi_{\text{plane}}(n_p) = \left|\frac{1}{n_{\text{bin}}}\sum_{j=1}^{n_{\text{bin}}}\exp\{i[2\pi(n_p-1)/L_p]p_j\}\right|, \quad (6)$$

with

$$p_j \in \{y_j, z_j\}, \quad L_p \in \{L_y, L_z\}. \quad (7)$$

This plane order parameter is unity if the particles are distributed in n_P equidistant planes over the channel.

D. Bond orientational order parameter

To analyze the structure of 2D systems the local bond orientational order parameter Ψ_6 is calculated which measures the angle between a particle and its nearest neighbors and is defined as

$$\Psi_6 = \frac{1}{m}\sum_{k=1}^{m} \exp\{i6\Theta_k\}, \tag{8}$$

where m is the number of neighbors of a given particle and Θ_k is the angle between the vector connecting the particle with its kth neighbor and an arbitrary reference axis. In a lattice with sixfold symmetry the angle is 60° and the order parameter is unity while for a fluid it is zero.

In a 3D system the local orientational symmetries can be determined by using the bond orientational parameters (bops) $\hat{Q}_l$ and $\hat{W}_l$ [33]. The former parameters are defined as

$$\hat{Q}_l = \left[\frac{4\pi}{2l+1}\sum_m |\hat{Q}_{lm}|^2\right]^{1/2}, \tag{9}$$

with the average over nearest neighbors N_b,

$$\hat{Q}_{lm} = \frac{1}{N_b}\sum_{bonds} Q_{lm}(\mathbf{r}), \tag{10}$$

$$Q_{lm}(\mathbf{r}) = Y_{lm}(\theta(\mathbf{r}), \phi(\mathbf{r})), \tag{11}$$

with the spherical harmonics $Y_{lm}(\theta,\phi)$, where $\theta(\mathbf{r})$ and $\phi(\mathbf{r})$ are the polar angles of the distance $\mathbf{r}$ connecting two nearest neighbors with respect to some reference coordinate system. The latter parameters are defined as

$$\hat{W}_l = \frac{\sum_{\substack{m_1,m_2,m_3 \\ m_1+m_2+m_3=0}} \begin{bmatrix} l & l & l \\ m_1 & m_2 & m_3 \end{bmatrix} \times \hat{Q}_{lm_1}\hat{Q}_{lm_2}\hat{Q}_{lm_3}}{\left[\sum_m |\hat{Q}_{lm}|^2\right]^{3/2}}, \tag{12}$$

where the coefficients are the Wigner $3j$ symbols. Nearest neighbors are determined by

$$C_N = 1.2\ \max\{a_x, a_y, a_z\}, \tag{13}$$

with the particle separations a_x, a_y, and a_z. In an ideal fcc or hcp lattice the particle separations are equal, $a_x = a_y = a_z$, and are connected to the distance between adjacent planes d_i in x, y, and z directions via

$$a_x = d_x, \quad a_y = \frac{2}{\sqrt{3}}d_y, \quad a_z = \sqrt{\frac{3}{2}}d_z. \tag{14}$$

However, if the system is confined, e.g., in a microchannel, the particle separations deviate from those in an ideal hcp or fcc lattice: (i) the ratios d_x/d_y and d_x/d_z, which we refer to as lattice stretching parameters in the following, adjust to the given boundary condition leading to a lattice that is distorted compared to an ideal lattice and (ii) for equal boundary conditions in y and z directions the plane distances in these directions are equal, $d_y = d_z$. From Table I it is clear that the values of the bops change upon changing the lattice stretching parameter d_x/d_y or d_x/d_z. The dependence of the bops $\hat{Q}_{l=4}$ and $\hat{W}_{l=4}$ on the lattice stretching parameter d_x/d_y is shown in Fig. 1 calculated for a fcc or hcp lattice with $d_y = d_z$ and varying the particle separation in the x direction.

TABLE I. Calculated values of the bond orientational order parameters $\hat{Q}_l$ and $\hat{W}_l$ for $l=4$ and $l=6$ for ideal crystal structures ($a_x = d_x > d_y = \sqrt{3}/2d_x > d_z = \sqrt{2/3}d_x$ for hcp and fcc lattices), elongated hcp and fcc lattices ($a_x = d_x > d_y = d_z = \sqrt{3}/2d_x$), and a compressed lattice ($a_x = d_x = d_y = d_z$). Values* are from [33].

	$\hat{Q}_{l=4}$	$\hat{Q}_{l=6}$	$\hat{W}_{l=4}$	$\hat{W}_{l=6}$
Liquid	0	0	0	0
		Ideal crystal structure		
hcp	0.0972222	0.484762	0.134097	−0.012442
fcc	0.190941	0.574524	−0.159317	−0.0131606
bcc	0.03637	0.51069	−0.159317	0.013161
sc*	0.76376	0.35355	0.159317	0.013161
icos*	0	0.66332	0	−0.169754
		Elongated crystal structure		
hcp	0.12537	0.488371	0.134097	−0.0125585
fcc	0.19436	0.571496	−0.140789	−0.0131637
		Compressed crystal structure		
hcp	0.169816	0.477932	0.142372	−0.00967825
fcc	0.215232	0.552729	−0.0431347	−0.010836

The strong dependence of the bops on the lattice stretching parameter shows that it is not possible to determine the local crystal structure from the values of the bops of an ideal crystal structure alone. Rather, the value d_x/d_y has to be determined first. The value of the bops at that ratio determines the local crystal structure.

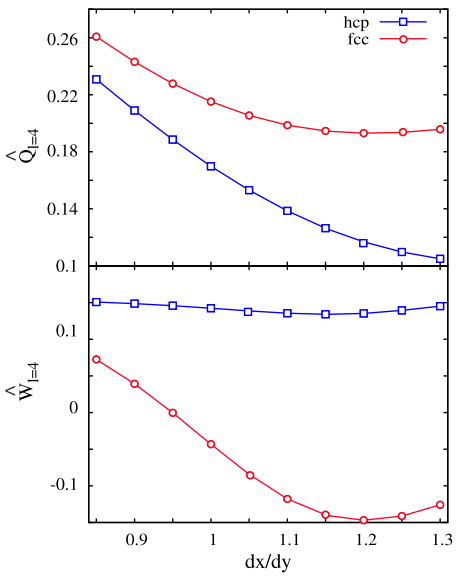

FIG. 1. (Color online) Bond orientational order parameters $\hat{Q}_{l=4}$ and $\hat{W}_{l=4}$ as functions of the lattice stretching parameter d_x/d_y for hcp (open squares) and fcc (open circles) lattices.

TABLE II. Parameter used for the Yukawa hard-core (YHC) interaction potential for colloidal systems in the 2D microchannels. U is the contact value, κ is the inverse Debye screening length, and n_L is the number of layers in the channel after 10^6 time steps with an external force $F^{\text{ext}}=2.603\times10^{-15}$ N. The bold numbers denote the number of layers in equilibrium ($F^{\text{ext}}=0$), $\nabla\rho$ is the density gradient, and v_D is the average drift velocity in the stationary nonequilibrium. The drift velocity of noninteracting particle in the external field has a value of $v_D=6.07\times10^{-8}$ m/s [Eq. (15)].

System	U	$\kappa\sigma$	$\rho\sigma^2$	n_L	$\nabla\rho$	v_D (10^{-8} m/s)
1	400	4	0.4	8,**7**	0	6
2	800	4	0.4	8,**7**	0	6
3	1000	4	0.4	8,**7**	0	6
4	800	8	0.5	8	0	6
5	432.45	1.015	0.4	8,**7**,6	$\neq0$	11

III. RESULTS AND DISCUSSION

A. Layer reduction in 2D microchannels

Starting from a system of YHC particles in a 2D channel with an inverse Debye screening length $\kappa\sigma=4$ and a contact value $U=400$, the values of the interaction potential are varied. The transport behavior of the confined particles is investigated, i.e., the colloids are driven by the application of an external driving force $\mathbf{F}^{\text{ext}}=F^{\text{ext}}\mathbf{e}_x$ through the channel forming a system in nonequilibrium. The results are summarized in Table II. In agreement with the results from [14] we find a longitudinal density gradient and consequently a layer transition for particle interaction ranges larger than the average particle separation. We calculate the average overall drift velocity for the different values of the interaction potential. If the particle flow is dominated by the driving force, i.e., in the regime of plug flow, the particles move with

$$\langle \Delta v_{\text{drift}} \rangle_{\text{Drude}} = \frac{F^{\text{ext}}}{\xi}, \tag{15}$$

as expected for noninteracting particles. This dependency was formulated for the transport of electrons in a metal by Drude [34]. For large screening ($\kappa\sigma>4$) the average velocity of a particle in the channel corresponds to the velocity of noninteracting particles [Eq. (15)]. Hence, the driving force dominates and we find plug flow of the particles without layer reduction. In most of the regions the particles arrange themselves in a hexagonal order. The formation of this order naturally gives rise to the formation of layers in flow direction similar to the layering phenomenon observed under equilibrium conditions [19,20]. Still, a local increase in the number of layers formed in equilibrium occurs due to an increase in the local density, which is caused by the boundary conditions. For low screening ($\kappa\sigma\leq1.025$) the range of the interaction potential is on the order of the particle separation and the particles move faster than expected. The reason is that the Drude model is based on a friction-dependent mobility only. However, for low screening the diffusion of the particles has to be taken into account and the interplay of a small drift and the diffusion gives rise to an increased mobility in the x direction. The system shows essentially the same features as the system of superparamagnetic particles [13,14]: we find rearrangement of the particles to a nearly hexagonal lattice and the occurrence of layer reduction under non-plug-flow conditions. A typical simulation snapshot of the defect configuration around the points where a change in the number of layers occurs is shown in Fig. 2. The system is nearly hexagonal in left and right of the point of layer reduction. The reduction in the number of layers gives rise to a defect. In the stationary nonequilibrium after about 2×10^6 time steps the position of the layer reduction zone does not move with the particles in flow direction. The particles move dynamically in layers adapting to the external force. The local particle densities and the particle separations are shown in Fig. 3(a) and the number of layers is shown in terms of the layer order parameter [Eq. (5)] in Fig. 3(b). A continuous density gradient forms along the channel. At the left end of the channel where eight layers form the particle separation a_x is larger than a_y. The lattice is compressed perpendicular to the confining walls since an additional layer forms compared to the equilibrium configuration. At the point of layer reduction the value of a_y shows a jump to a higher value. At the same time the value of a_x decreases and a_x is smaller than a_y at the transition point. While a_y remains constant until the next reduction point, a_x increases monotonically until the value is so large that another reduction occurs. Stretching of the lattice in flow direction leads to an instability toward a smaller number of layers. At the transition point the changes in a_x and a_y compensate each other leading to the continuous

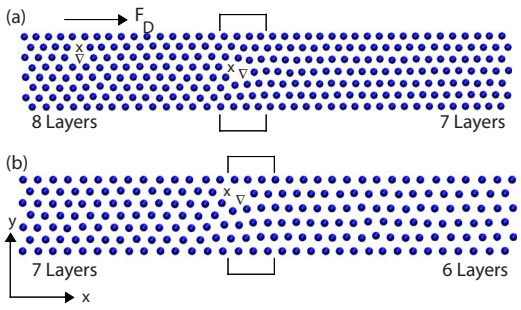

FIG. 2. (Color online) Simulation snapshots of the defect configuration for a YHC system ($\kappa\sigma=1.015$, $U=432.45$) in a 2D channel with ideal hard walls. The rectangles mark the region of the layer reduction. Full circles (●) mark bulk particles with six nearest neighbors and particles at the wall with four nearest neighbors. Symbol × corresponds to a fivefold symmetry and symbol ▽ corresponds to a sevenfold symmetry.

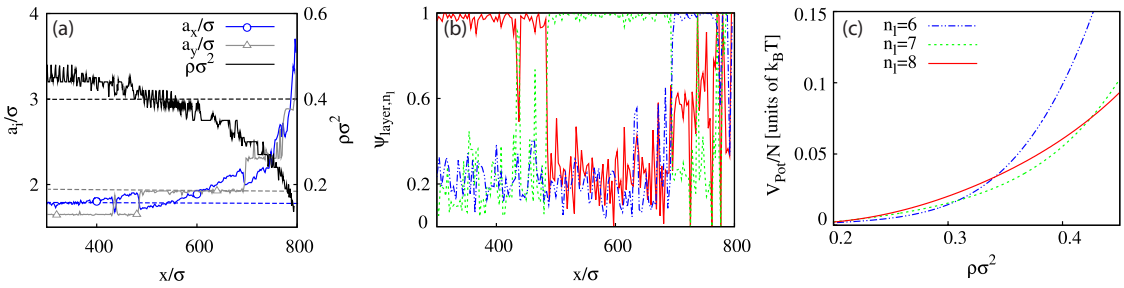

FIG. 3. (Color online) (a) Local particle density and local particle separations a_x and a_y in the stationary nonequilibrium. The dashed lines indicate the values in equilibrium. (b) Layer order parameter of the configuration shown in Fig. 2. (c) Potential energies per particle of different layer configurations as a function of the particle density.

decrease in the density. The reduction in the number of layers can be explained qualitatively by calculating the potential energy per particle in dependence of the local density: starting from an ideal triangular lattice with a constant number of layers, the particle separations in the x direction are varied and the potential energy per particle is calculated in dependence of the local density. The potential energy, shown in Fig. 3(c) for a different number of layers, has clear intersection points. For an in the x-direction stretched configuration with n_l layers it can therefore become energetically favorable to switch to a configuration with (n_l-1) layers. Below a local density of $\rho\sigma^2=0.31$ it is energetically favorable for the system to form six layers; for a density between $0.31<\rho\sigma^2<0.425$ seven layers are energetically favorable, while above $\rho\sigma^2=0.425$ eight layers are energetically favorable. These densities are in good agreement with the values at which a reduction in the number of layers is observed in the simulations.

B. Three-dimensional colloidal systems in equilibrium

To study the influence of parallel walls confining a 3D system in y and z directions we first simulate an unconfined system using a cubic simulation box and periodic boundary conditions in all directions. The static structure factor $S(k)$ is calculated from the Fourier-transformed radial distribution function $g(r)$, where k is the wave vector. The value of the first peak exceeds the value of 2.85 at which the system is melting according to the Hansen-Verlet criterion [35], indicating that the system is in the crystal phase. The local crystal structure was determined using the bops $\hat{Q}_{l=4}$ and $\hat{W}_{l=4}$. The results for the unconfined system as well as for systems confined within microchannels of different square sections are summarized in Table III: for both the unconfined and the confined systems a random hexagonal close packed (rhcp) structure forms in equilibrium, i.e., a random mixture of areas with particles showing a fcc or hcp symmetry in agreement with experimental results [36,37]. Note that for a hard-sphere system, which behaves similar to the YHC system, the fcc structure is favored by only $(9\pm2)\times10^{-4}k_BT$ per particle compared to the hcp structure [38,39] leading to stacking defects. In the following we discuss the structural changes upon confining the 3D system in a microchannel with a square cross section.

C. Transverse mobility at the channel walls

The influence of the channel width on the emerging structure in 3D systems is similar to the 2D case discussed in [14,19,28,29]. For small cross sections the structure depends strongly on the channel width. Small changes in the distance between the walls leads to significant structural changes mirrored in the mean-square displacement (MSD) perpendicular

TABLE III. Local crystal structure of YHC particles ($\kappa\sigma=1.015$, $U=432.45$) for selected 3D channels of width w with n_P planes and average lattice stretching parameter $\bar{d}_x/\bar{d}_y$ and the unconfined system. The local crystal structure is determined using bond orientational order parameters and the percentage of particles with fcc symmetry, p_{fcc}, or hcp symmetry, p_{hcp}, is given as well as the percentage of defects p_{Def}, i.e., the number of particles which have values of the bops that correspond neither to fcc symmetry nor to hcp symmetry.

w (σ)	n_P	$\bar{d}_x/\bar{d}_y$	p_{fcc} (%)	p_{hcp} (%)	p_{Def} (%)
4.5	4	1.15	50.8	32.2	17.0
5.0	4	0.98	74.5	20.9	5.0
5.5	5	1.21	57.0	14.8	28.1
5.7	5	1.16	52.5	21.6	26.0
6.3	5	1.03	66.3	19.6	14.2
6.9	6	1.17	53.0	26.0	21.0
9.3	8	1.15	51.1	24.1	24.8
Unconfined		1.13	49.9	19.2	31.0

to the wall, the density profile, and has an influence on the number of defects in the crystal structure. With increasing channel width these structural quantities oscillate indicating magic numbers of the channel width for which the structure is particularly stable. For these channels the structure is almost identical to the structure of the unconfined system.

The dimensionless mean-square displacement perpendicular to the wall $\langle \Delta\tilde{y}^2(\tilde{\tau})\rangle$ or $\langle \Delta\tilde{z}^2(\tilde{\tau})\rangle$ of particles localized close to the wall in dependence of the lag time $\tilde{\tau}$ is a measure of their transverse mobility. Here, we refer to wall particles if their distances from the wall are smaller than their diameters σ. After about 10^5 time steps the mean-square displacement reaches a plateau value. Hence, particles located close to the wall will remain in vicinity of the wall for a significantly long time. To calculate the MSD in dependence of the dimensionless channel width $\tilde{w}$ and the dimensionless position $\tilde{y}$ close to the wall, the interaction potential is divided into a sum consisting of the contributions of the particles in the same layer $\tilde{V}_L$, the same plane $\tilde{V}_P$, and the same volume $\tilde{V}_V$,

$$\frac{V(\tilde{y},\tilde{w})}{k_BT} = \tilde{V}_L(\tilde{y},\tilde{w}) + \tilde{V}_P(\tilde{y},\tilde{w}) + \tilde{V}_V(\tilde{y},\tilde{w}). \tag{16}$$

The results for $\tilde{V}_L$ and $\tilde{V}_P$ are identical to the two-dimensional case from [19]. Since an analytical calculation of the MSD using the Yukawa interaction potential is not possible, the interaction potential between the particles is approximated by

$$\frac{V(r)}{k_BT} = U\left(\frac{\tilde{R}}{r}\right)^3, \tag{17}$$

with the interaction strength $U=241.2\pm2.7$ and the length scale $\tilde{R}$ (see below). Approximating particles close to the wall as a continuum, the three parts of the interaction potential can be expressed as

$$\tilde{V}_L(\tilde{y},\tilde{w}) = U\tilde{R}\tilde{\rho}_L\int_{-\infty}^{\infty}\frac{d\tilde{x}}{[\tilde{x}^2+(\tilde{c}-\tilde{y})^2]^{3/2}}, \tag{18}$$

$$\tilde{V}_P(\tilde{y},\tilde{w}) = U\tilde{R}^2\tilde{\rho}_P\int_{-\infty}^{\infty}\int_{2\tilde{c}}^{\tilde{w}}\frac{d\tilde{x}dY}{[\tilde{x}^2+(Y-\tilde{y})^2]^{3/2}}, \tag{19}$$

$$\tilde{V}_V(\tilde{y},\tilde{w}) = U\tilde{R}^3\tilde{\rho}\int_{-\infty}^{\infty}\int_{2\tilde{c}}^{\tilde{w}}\int_{2\tilde{c}}^{\tilde{w}}\frac{d\tilde{x}dYd\tilde{z}}{[\tilde{x}^2+(Y-\tilde{y})^2+\tilde{z}^2]^{3/2}}, \tag{20}$$

where $\tilde{c}$ is the position of the first peak in the density spectrum, i.e., the arbitrary cutoff between the different parts of the potential; $\tilde{\rho}_L$ is the dimensionless density of the particles within one line; and $\tilde{\rho}_P$ is the dimensionless density of the particles in the $(z=0)$ plane. Integration yields

$$\tilde{V}_L(\tilde{y},\tilde{w}) = \frac{2U\tilde{R}\tilde{\rho}_L}{(\tilde{c}-\tilde{y})^2}, \tag{21}$$

$$\tilde{V}_P(\tilde{y},\tilde{w}) = 2U\tilde{R}^2\tilde{\rho}_P\left(\frac{1}{2\tilde{c}-\tilde{y}}-\frac{1}{\tilde{w}-\tilde{y}}\right), \tag{22}$$

$$\tilde{V}_V(\tilde{y},\tilde{w}) = 2U\tilde{R}^3\tilde{\rho}\int_{2\tilde{c}}^{\tilde{w}}d\tilde{z}\frac{\arctan\left(\frac{\tilde{w}-\tilde{y}}{\tilde{z}}\right)-\arctan\left(\frac{2\tilde{c}-\tilde{y}}{\tilde{z}}\right)}{\tilde{z}}$$

$$\le 2U\tilde{R}^3\tilde{\rho}\left((\tilde{w}-2\tilde{c})\frac{\arctan\left(\frac{\tilde{w}-\tilde{y}}{2\tilde{c}}\right)}{2\tilde{c}}-\int_{2\tilde{c}}^{\tilde{w}}d\tilde{z}\frac{2\tilde{c}-\tilde{y}}{\tilde{z}^2}\right) \tag{23}$$

$$=2U\tilde{R}^3\tilde{\rho}\left[\frac{\arctan\left(\frac{\tilde{w}-\tilde{y}}{2\tilde{c}}\right)}{2\tilde{c}}-(\tilde{y}-2\tilde{c})\left(\frac{1}{\tilde{w}}-\frac{1}{2\tilde{c}}\right)\right]. \tag{24}$$

The expression for the potential can be expanded to first order near $\tilde{y}=0$,

$$\tilde{V}(\tilde{y},\tilde{w}) \approx A(\tilde{c},\tilde{w}) + B(\tilde{c},\tilde{w})\tilde{y}, \tag{25}$$

with

$$A(\tilde{c},\tilde{w}) = \frac{2U\tilde{R}\tilde{\rho}_L}{\tilde{c}^2} + 2U\tilde{R}^2\tilde{\rho}_P\left(\frac{1}{2\tilde{c}}-\frac{1}{\tilde{w}}\right) + 2U\tilde{R}^3\tilde{\rho}\left[\left(\frac{\tilde{w}}{2\tilde{c}}-1\right)\arctan\left(\frac{\tilde{w}}{2\tilde{c}}\right)+\left(1-\frac{2\tilde{c}}{\tilde{w}}\right)\right], \tag{26}$$

$$B(\tilde{c},\tilde{w}) = \frac{4U\tilde{R}\tilde{\rho}_L}{\tilde{c}^3} + 2U\tilde{R}^2\tilde{\rho}_P\left(\frac{1}{\tilde{w}^2}-\frac{1}{4\tilde{c}^2}\right) - 2U\tilde{R}^3\tilde{\rho}\left[\frac{\frac{\tilde{w}}{2\tilde{c}}-1}{2\tilde{c}+\frac{\tilde{w}^2}{2\tilde{c}}}-\left(\frac{1}{\tilde{w}}-\frac{1}{2\tilde{c}}\right)\right]. \tag{27}$$

In the long-time limit the canonical ensemble average of the MSD reads

$$\lim_{\tilde{\tau}\to\infty}\langle\Delta\tilde{y}^2\rangle(\tilde{c},\tilde{w}) = 2\langle\tilde{y}^2\rangle(\tilde{c},\tilde{w}) - 2\langle\tilde{y}\rangle^2(\tilde{c},\tilde{w}) = 2\frac{\int_0^{\epsilon}\tilde{y}^2e^{-A-B\tilde{y}}d\tilde{y}}{\int_0^{\epsilon}e^{-A-B\tilde{y}}d\tilde{y}} - 2\left(\frac{\int_0^{\epsilon}\tilde{y}e^{-A-B\tilde{y}}d\tilde{y}}{\int_0^{\epsilon}e^{-A-B\tilde{y}}d\tilde{y}}\right)^2. \tag{28}$$

The upper integration limit can be replaced with infinity since the Boltzmann factor drops quickly to zero and the MSD reads

$$\lim_{\tilde{\tau}\to\infty}\langle\Delta\tilde{y}^2\rangle(\tilde{c},\tilde{w}) = \frac{4}{B^2}-\frac{2}{B^2} = \frac{2}{B^2}. \tag{29}$$

The dependence of the position of the first peak in the density profile $\tilde{c}$ on the channel width $\tilde{w}$ can be approximated by

$$\tilde{c} \approx \tilde{R}\left(1+\frac{1}{\tilde{w}}\right), \tag{30}$$

where $\tilde{R}$ is the dimensionless effective boundary plane distance, which is calculated from the density profiles from the simulations. Due to reduced neighbor interaction at the wall the effective boundary plane distance deviates from the distance between adjacent planes in an ideal unconfined system. Using Eqs. (30), (29), and (27) yields the MSD normal to the wall:

$$\lim_{\tilde{\tau}\to\infty}\langle\Delta\tilde{y}^2\rangle(\tilde{c},\tilde{w}) = \frac{1}{2U^2}\left(\frac{2\tilde{\rho}_L}{\tilde{R}^2\left(1+\frac{1}{\tilde{w}}\right)^3}+\frac{\tilde{R}^2\tilde{\rho}_P}{\tilde{w}^2}+\frac{\tilde{R}^2\tilde{\rho}_P}{4\tilde{R}^2\left(1+\frac{1}{\tilde{w}}\right)^2}-\frac{\frac{\tilde{R}^3\tilde{\rho}\tilde{w}}{2\tilde{R}\left(1+\frac{1}{\tilde{w}}\right)}-\tilde{R}^3\tilde{\rho}}{2\tilde{R}\left(1+\frac{1}{\tilde{w}}\right)+\frac{\tilde{w}^2}{2\tilde{R}\left(1+\frac{1}{\tilde{w}}\right)}}+\frac{\tilde{R}^3\tilde{\rho}}{\tilde{w}}-\frac{\tilde{R}^3\tilde{\rho}}{2\tilde{R}\left(1+\frac{1}{\tilde{w}}\right)}\right)^{-2}. \tag{31}$$

For large channel widths Eq. (31) can be expanded to

$$\lim_{\tilde{\tau}\to\infty}\langle\Delta\tilde{y}^2\rangle(\tilde{c},\tilde{w}) \simeq \frac{1}{2U^2\left(\frac{2\tilde{\rho}_L}{\tilde{R}^2}+\frac{\tilde{\rho}_P}{4}-\frac{\tilde{R}^2\tilde{\rho}}{2}\right)^2}\left(1-\frac{2\left[-\frac{6\tilde{\rho}_L}{\tilde{R}^2}-\frac{\tilde{\rho}_P}{2}-\tilde{\rho}\tilde{R}^3+\tilde{R}^3\tilde{\rho}\left(1+\frac{1}{2\tilde{R}}\right)\right]}{\frac{2\tilde{\rho}_L}{\tilde{R}^2}+\frac{\tilde{\rho}_P}{4}-\frac{\tilde{R}^2\tilde{\rho}}{2}}\frac{1}{\tilde{w}}\right). \tag{32}$$

Figure 4 shows the plateau values of the MSD from the Brownian dynamics simulations of channels with different square sections and the analytical result from Eqs. (31) and (32). The analytical expression is fitted to the simulation results using the fit parameter $U_{\mathrm{Fit}}=58.13\pm0.44$. Due to the approximations the fit parameter deviates from the interaction strength U. Still, the qualitative behavior of the simulation results is well captured. For large channels the MSD reaches a constant value with a correction of the order $1/\tilde{w}$. The dependence of the MSD on the channel width reveals that the important factor to the MSD comes from the interaction of the wall particles with immediate neighboring particles, while the interaction with particles further away gives a contribution of higher order only explaining the surprising finding that the dependence of the MSD on the channel width is the same in 3D as in 2D microchannels.

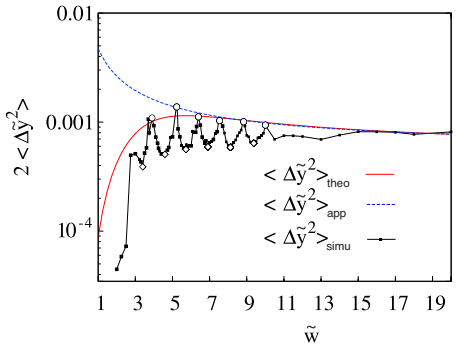

FIG. 4. (Color online) Plateau values of the mean-square displacement of wall particles in direction normal to the walls of a 3D channel in dependence of the dimensionless channel width $\tilde{w}$. Minima correspond to the magic channels (open diamonds) and maxima correspond to an integer multiple of the effective boundary plane distance $R=1.2718\sigma$ (open circles). The lines show the analytical result for the mean-square displacement according to Eq. (31) (red solid line) and the approximation for large channel width according to Eq. (32) (blue dashed line).

The plateau values from the simulations show oscillations occurring likewise in y and z directions. These oscillations vanish for $w\geq 11\sigma$ indicating that the effects leading to the periodic alteration of the MSD occur in the center of the channel and do not affect the wall particles for large channel widths. For channel widths being an integer multiple of R the MSD shows maxima. In this case a loose structure forms within the channel in which the wall particles can move away from the wall easily. Minima of the MSD occur at the channel widths 3.4σ, 4.5σ, 5.7σ, 6.9σ, 8.1σ, and 9.3σ. These "magic numbers" for the widths do not emerge at integer multiples of the plane distance as expected. Calculating the average values of the particle separations reveals that in this case $\bar{a}_x=\bar{a}_y=\bar{a}_z$ and the average lattice stretching parameter $\bar{d}_x/\bar{d}_y$ corresponds to that of the unconfined system. In contrast, if the MSD shows a maximum, the particle separations are unequal ($\bar{a}_x\neq\bar{a}_y\neq\bar{a}_z$). In this case the lattice stretching parameter $\bar{d}_x/\bar{d}_y$ is smaller than in an unconfined system. Hence, a loose structure forms if the lattice is stretched perpendicular to the walls confining the system.

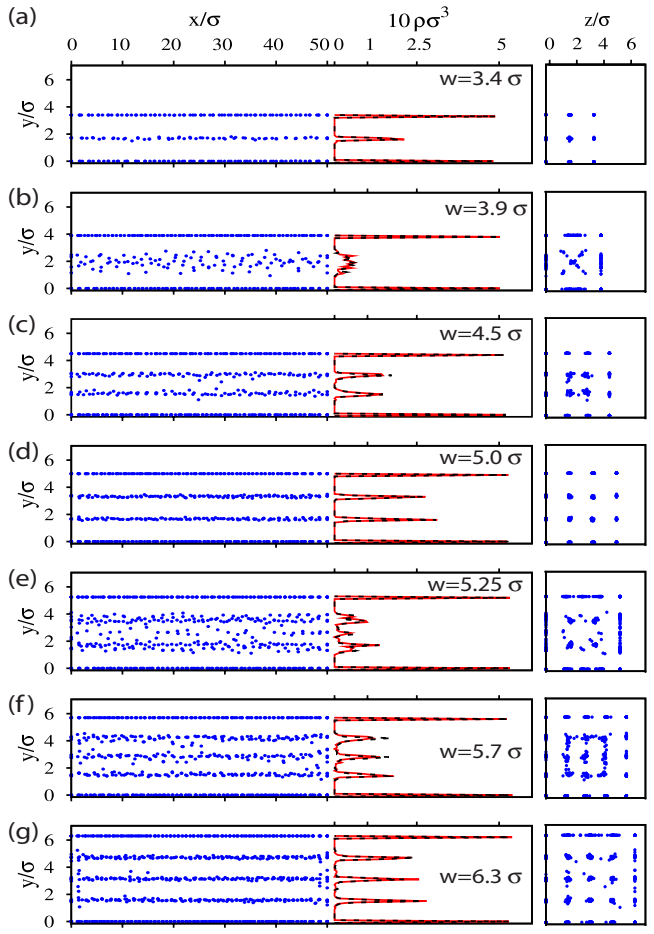

FIG. 5. (Color online) Projection of simulation snapshots of the equilibrium configuration of YHC system ($\kappa\sigma$=1.015, U =432.45) in 3D microchannels on the xy plane for different channel widths (left) and average density profile (middle) in y direction [red (light gray) line] and z direction (black line). The projection of the equilibrium configuration on the yz plane is shown to the right.

D. Density profile

To analyze the structure of systems in more detail the density profile is calculated. Figure 5 shows the density profile perpendicular to the confining walls in y and z directions as well as simulation snapshots of the equilibrium configuration. One characteristic property of the density profile is the increased peak at the channel wall which results from the fact that it is energetically favorable to distribute the particles in such a way that particles with less nearest neighbors close to the wall have smaller separations than those with more neighbors in the center of the channel. This is also the reason why the distance of the first plane from the wall is smaller than the distance of adjacent planes in the center of the channel. The origin of the oscillations in the structural properties is apparent from the configuration snapshots (Fig. 5): for channel widths smaller than 2σ two planes form—one at each wall. With increasing square section w the particles start to occupy the center of the channel forming a stable midplane at $w \approx 3.4\sigma$. This plane forces the wall particles to remain close to the wall, thus leading to a minimum in the MSD. If the channel width is further increased the interaction between particles in adjacent planes decreases leading to an increase in the MSD until the midplane splits up into two planes and the MSD shows a second minimum at $w=4.5\sigma$. Until a channel width of $w=5$ the distance between the planes increases while the particle separation in the x direction decreases. Therefore, the lattice is stretched perpendicular to the confining walls and the MSD shows a maximum. Above $w=5.25\sigma$ the particle separations in the x direction are so small that it is energetically favorable to form an additional plane. This process continues up to a channel width of $\sim 11\sigma$ whereas maxima in the MSD occur if the distance between adjacent planes is maximal, i.e., if the lattice is stretched normal to the confinement and the interaction between the particles in adjacent planes is minimal. Minima of the MSD occur if an ideal undistorted lattice can form.

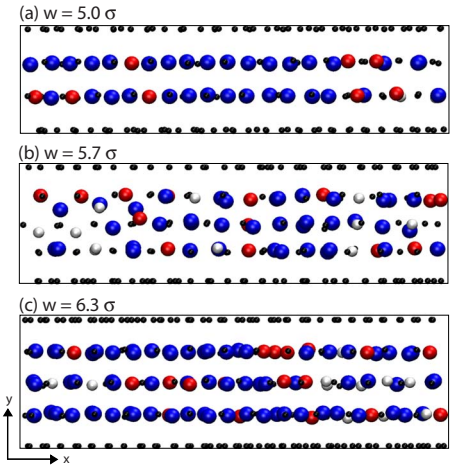

FIG. 6. (Color online) Local crystal structure in 3D microchannels for selected channel widths. Particles with fcc symmetry are blue (dark gray), those with hcp symmetry are red (light gray), and defects are white. Wall particles are shown as small black spheres for clarity.

E. Crystal structure in dependence of the channel width

The local crystal structure within channels of different square sections is determined using the values of the bops $\hat{Q}_{l=4}$ and $\hat{W}_{l=4}$ at the appropriate lattice stretching parameter d_x/d_y (Fig. 1). The results are summarized in Table III and a snapshot of the local crystal structure is shown in Fig. 6 for selected channel widths. Wall particles with a distance $d < \sigma$ from the wall are neglected, as they have different values of the bops due to missing next neighbors [33]. For all systems $\hat{Q}_{l=4} > 0.0364$ and $\hat{W}_{l=6} < 0$ indicating that there are no particles with bcc symmetry. In the magic channels a rhcp structure forms as in the unconfined system with a larger fcc proportion ($\sim$50%) than hcp proportion ($\sim$20%) in the equilibrium crystal structure [Fig. 6(b)]. For channel widths where the lattice is stretched normal to the confinement (maxima of MSD) a rhcp structure forms, too [Figs. 6(a) and 6(c)]. However, the number of defects is smaller, as the particles are more localized within one plane and the fcc proportion is larger than in the magic channels. For channel

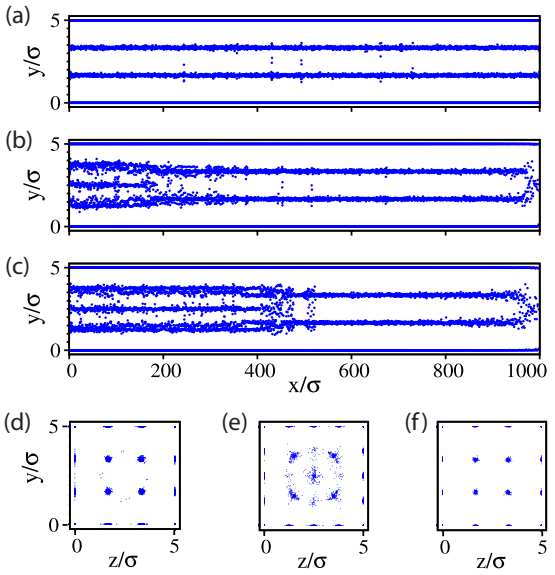

FIG. 7. (Color online) Projection of simulation snapshots of the configuration in a 3D microchannel on the xy plane (a) in equilibrium without an external force, (b) after 10^5 time steps with an external driving force, and (c) in the stationary nonequilibrium after 10^6 simulation steps with a constant position of the plane reduction zone within the channel. Projection of simulation snapshots on the yz plane (d) for the equilibrium configuration, (e) for the configuration in the stationary nonequilibrium in the region before the reduction zone, and (f) after the reduction zone. For clarity all distances in y direction are stretched by a factor of 16 in the xy projection.

width larger than 11σ the lattice can hardly be influenced by the distance between parallel walls. A different possibility to influence the structure is the application of an external field, which will be discussed in the following.

F. Transport behavior of colloids in 3D microchannels

Now, we want to address the transport behavior of colloids confined in a 3D microchannel. Again, the colloids are driven by the application of an external driving force. First, we focus on the effect of a reduction in the number of planes, i.e., the dynamical rearrangement of the colloids during their flow along the channel. This phenomenon is analogous to the layer reduction observed in the 2D microchannels. Figure 7(a) shows the equilibrium configuration in a 3D channel with a quadratic square section of width $w=5\sigma$ and length 1000σ. In equilibrium a loose structure with four planes forms, which is stretched perpendicular to the confinement and in which the particles can move away from the wall easily [see Figs. 5(d) and 6(a) and Table III]. In the stationary nonequilibrium the average drift velocity is 1.43×10^{-7} m/s, which is significantly larger than the drift velocity of noninteracting particles [Eq. (15)] indicating non-plug-flow. Figure 7 shows the time evolution of the system: in equilibrium a plane structure forms with four planes parallel to the confining walls in y and z directions. The external force leads after 10^5 time steps to an additional fifth plane in the reservoir. The area with five planes moves with increasing time in flow direction. Close to the end of the channel the number of planes reduces from four to three planes. After 10^6 time steps the system reaches a stationary nonequilibrium. After that time the position, at which a reduction in the number of planes occurs, does not move in flow direction any more. The transition point oscillates backward and forward within a small area. The particles move in planes and layers adapting to the external force. At the transition point the particles have to switch from the midplane to one of the adjacent planes closer to the channel wall. Often, particles leave the midplane and proceed in flow direction before changing on a plane further outside. The local particle densities and the particle separations are shown in Fig. 8(a) and the number of planes is shown in terms of the plane order parameter [Eq. (6)] in Fig. 8(b). In the stationary nonequilibrium a density gradient forms along the complete length of the channel causing the change in the number of planes and therefore leading to a change in the particle separations. At the left end of the channel the particle separation a_x is larger than a_y and a_z, and the lattice is compressed perpendicular to the confinement. In the transition area a_y and a_z increase in two steps in contrast to the 2D systems where the particle separation a_y shows a single jump. At the end of the transition area a_x is smaller than a_y and a_z. While the latter two remain constant until the next transition point, a_x increases monotonically. This behavior suggests that stretching of the lattice in flow direction leads to an instability causing the reduction in the number of planes. The change in the number of planes is clearly visible from the plane order parameter

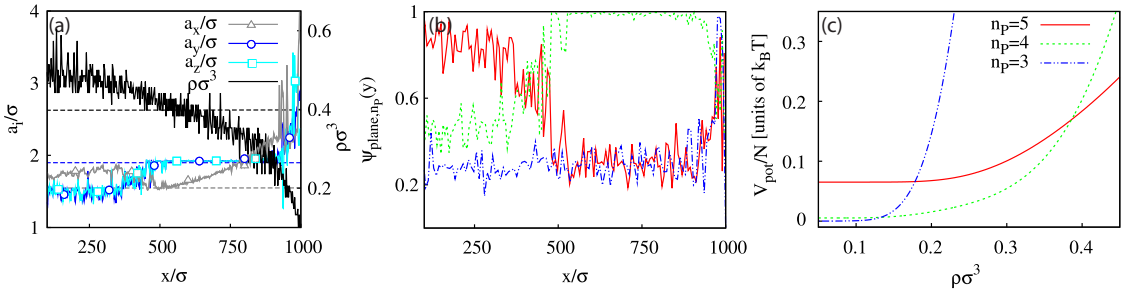

FIG. 8. (Color online) Difference of the potential energy per particle in a hcp and a fcc lattice. (a) Local density distribution within the channel and particle separations a_x, a_y, and a_z in the stationary nonequilibrium after 10^6 time steps. The dashed lines show the equilibrium values of the local density and the particle separations. (b) Plane order parameter of the configuration shown in Fig. 7(c). (c) Potential energy for a fcc lattice in a channel of width 5σ in dependence of the local density for the number of planes in the stationary nonequilibrium.

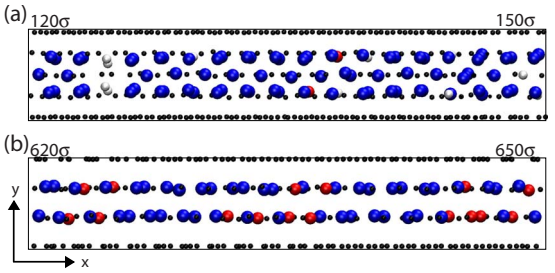

FIG. 9. (Color online) Local crystal structure in the stationary nonequilibrium (a) in the region with an additional fifth plane $120\sigma < x < 150\sigma$ and (b) in the region with four planes $620\sigma < x < 650\sigma$. Particles with fcc symmetry are blue (dark gray), those with hcp symmetry are red (light gray), defects are white, and wall particles are shown as small black spheres for clarity.

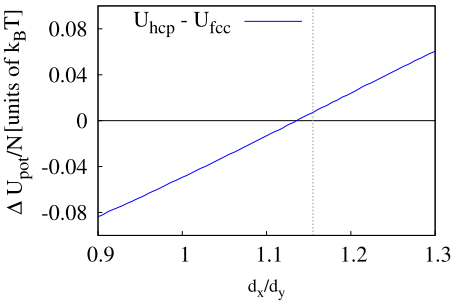

FIG. 10. (Color online) Difference of the potential energy per particle in a hcp and a fcc lattice, $\Delta V = V_{\mathrm{hcp}} - V_{\mathrm{fcc}}$, in dependence of the lattice stretching parameter d_x/d_y. The dashed line indicates the value of d_x/d_y of an ideal fcc lattice.

shown in Fig. 8(b). The order parameter does not have a sharp transition point but rather a transition area with an extension of about 100σ in which the value changes steplike. The reason is that the order parameter of the wall particles drops to zero about 100σ later than the order parameter of the planes in the middle of the channel. Thus, the planes closest to the wall are more stable against a deformation of the lattice. Again, the reduction in the number of planes can be explained by calculating the potential energy per particle in dependence of the local density. Starting from an ideal fcc crystal with a constant number of planes, i.e., constant distances between the particles in y and z directions, the distances in the x direction are increased or decreased, and the potential energy is calculated. The dependence of the potential energy on the local density for a constant number of planes is shown in Fig. 8(c). Above a value of the local density of $\rho\sigma^3 = 0.38$ it is energetically favorable for the system to form five planes; for values $0.38 > \rho\sigma^3 > 0.13$ four planes are energetically favorable and below $\rho\sigma^3 = 0.13$ three planes are energetically favorable. These values are slightly smaller than the values at which a reduction occurs in the simulations. This can be explained by the fact that the density in the middle of the channel is smaller than close to the walls (see Fig. 5).

G. Crystal structure in the stationary nonequilibrium

Figure 9 shows snapshots of the crystal structure which forms in the stationary nonequilibrium in the region of the channel with five planes [Fig. 9(a)] and with four planes [Fig. 9(b)]. In both regions a rhcp structure forms as in the equilibrium configuration. The fcc and hcp proportions in the crystal structure change in dependence of the lattice stretching parameter d_x/d_y. The dependence of the potential energy difference per particle in a hcp and a fcc lattice $\Delta U_{\mathrm{pot}} = U_{\mathrm{hcp}} - U_{\mathrm{fcc}}$ on the lattice stretching parameter d_x/d_y is shown in Fig. 10. On the left-hand side of the channel an additional fifth plane forms and the lattice is compressed normal to the confinement. The stretching parameter has a value of $d_x/d_y = 1.3$, which is significantly larger than in the equilibrium configuration. For this ratio the potential energy per particle of a fcc crystal is $0.0623 k_B T$ smaller than that of a hcp lattice. In the crystal structure the hcp proportion (7.7%) is suppressed in favor of the fcc proportion (78.3%). At the same time the number of defects increases (14%) compared to the number of defects in equilibrium. In the region with four planes the lattice stretching parameter has a value of $d_x/d_y = 1.02$ and the potential energy of the hcp lattice is smaller compared to the fcc lattice. The crystal structure in this part of the channel is similar to the equilibrium configuration [Fig. 6(a) and Table III]. Most of the particles show a fcc symmetry (68%), some particles show a hcp symmetry (30%), and the number of defects is small (2%) since in the configuration with four planes the particles are more localized within one plane. Therefore, in the stationary nonequilibrium the number of planes is determined by the local density, while the crystal structure and the number of defects depend on the deformation of the lattice.

IV. SUMMARY

A structural analysis has been performed in a model system of charge stabilized colloids interacting via a YHC potential in 2D and 3D microchannels. We have reported on a variety of ordering and transport phenomena induced by the confinement of the motion of the particles by parallel walls and by the application of a constant driving force along the channel. We used Brownian dynamics simulations to analyze the structural behavior both under equilibrium and under stationary nonequilibrium conditions.

First, we have studied systems with varying interaction range in a 2D channel. A longitudinal density gradient and consequently a layer transition occur only for particle interaction ranges larger than the average distances between the neighboring particles in agreement with previous results [14]. Second, we have studied the systems in three dimensions. In an unconfined 3D system we observe a global rhcp structure in agreement with experimental results [36,37] as well as in the 3D microchannels where the motion of the particles is confined in all directions by ideal hard walls. In the microchannels closest packed (111) planes align parallel to the confining walls, leading to a plane structure with equal distances between adjacent planes in y and z directions for quadratic square sections of the channels. Systematically, we have analyzed the influence of the width of the channel on the MSD of the wall particles, the density profile, and the

local crystal structure. The structural properties show oscillations upon increasing the width of the channel with a period of the effective boundary plane distance. When the channel width is increased, a periodic destabilization of the plane structure with n_p planes takes place, and the system switches to a structure with (n_p+1) planes. Moreover, we have shown that the number of planes can be reduced by applying an external driving force. In the stationary nonequilibrium the particles flow over the reduction zone which stays at a constant position. For small driving forces, where the particles are not in the regime of plug flow, the particles arrange themselves into a different number of planes analogous to the rearrangement into layers in the 2D systems. The reduction originates from a density gradient along the channel and is similar to the system of driven superparamagnetic particles in 2D microchannels [13,14], suggesting that the phenomenon of layer reduction is independent of the exact form of the interaction potential and occurs likewise in 2D and 3D systems if the range of the interaction potential is larger than the average distance between neighboring particles. The local density decreases monotonically and continuously along the channel. In front of the reduction zone the lattice is stretched in flow direction whereas it is compressed and one layer or plane has disappeared after the reduction zone. Stretching of the lattice leads to an instability toward a decreased number of planes. At the point of reduction the increase in the particle separation a_y is compensated by the decrease in a_x, leading to a continuous decrease in the local density along the channel. In the 2D systems the change in the particle separations is jumplike while it has intermediate values in the 3D systems which result from the stabilization of the planes which are closest to the walls. The reduction in layers or planes takes place for specific values of the local density. Using a static stretching analysis the values of the local density can be calculated for which the transition from an energetically less favored longitudinal stretched lattice to a lattice with one layer or plane less occurs. The estimated values of the local density are in good agreement with the values from the simulations.

We have shown that the crystal structure of 3D colloidal systems can on one hand be manipulated by varying the geometry of the confinement or by applying an external force. Using a rather simple classical model system of colloidal particle interacting via a screened Coulomb potential allows us to predict both equilibrium properties and the transport behavior in confining geometries. The observed phenomena will take place in any system in which long-range interacting particles are driven by an external field through a narrow constriction. However, hydrodynamic interactions might modify the quantitative results for real microchannels whose dimensions are only a few particle diameters in magnitude: a particle close to a planar hard wall is subject to hydrodynamic interactions with the wall which enhance the transverse friction [40]. Moreover, for an array of interaction particles there is an additional enhancement of friction due to the hydrodynamic confining effect of the wall [41]. Another limitation of our approach is that an external driving force acting on the particles might lead to different results than pressure-driven flow since in the latter one a shear-induced tendency of twisting and disrupting the plane structure occurs [42]. Therefore, the results of these studies can be seen as a step in understanding transport processes in biological and quantum systems.

ACKNOWLEDGMENTS

We are grateful to S. Gerlach and P. Henseler for enjoyable discussions. We gratefully acknowledge support of the German Excellence Initiative via Elite Netzwerk Bayern (ENB) and via the International Doctorate Program NanoBioTechnology (IDK-NBT); the SFB 513; the SFB 767; the SFB TR6; and the NIC, HLRS, and SCC.

[1] H. Löwen, J. Phys.: Condens. Matter **13**, R415 (2001).
[2] R. Roth and D. Gillespie, Phys. Rev. Lett. **95**, 247801 (2005).
[3] T. M. Squires and S. R. Quake, Rev. Mod. Phys. **77**, 977 (2005).
[4] D. Helbing, P. Molnar, I. Farkas, and K. Bolay, Environ. Plan. B: Plan. Des. **28**, 361 (2001).
[5] M. Rex, H. Löwen, and C. N. Likos, Phys. Rev. E **72**, 021404 (2005).
[6] M. Rex and H. Löwen, Phys. Rev. E **75**, 051402 (2007).
[7] M. Rex and H. Loewen, Eur. Phys. J. E **26**, 143 (2008).
[8] J. Chakrabarti, J. Dzubiella, and H. Löwen, Phys. Rev. E **70**, 012401 (2004).
[9] J. Dzubiella and H. Löwen, J. Phys.: Condens. Matter **14**, 9383 (2002).
[10] J. Chakrabarti, J. Dzubiella, and H. Löwen, EPL **61**, 415 (2003).
[11] M. E. Leunissen, C. G. Christova, A.-P. Hynninen, C. P. Royall, A. I. Campbell, A. Imhof, M. Dijkstra, R. v. Roij, and A. v. Blaaderen, Nature (London) **437**, 235 (2005).
[12] K. R. Sütterlin, A. Wysocki, A. V. Ivlev, C. Räth, H. M. Thomas, M. Rubin-Zuzic, W. J. Goedheer, V. E. Fortov, A. M. Lipaev, V. I. Molotkov, O. F. Petrov, G. E. Morfill, and H. Löwen, Phys. Rev. Lett. **102**, 085003 (2009).
[13] M. Köppl, P. Henseler, A. Erbe, P. Nielaba, and P. Leiderer, Phys. Rev. Lett. **97**, 208302 (2006).
[14] P. Henseler, A. Erbe, M. Köppl, P. Leiderer, and P. Nielaba, Phys. Rev. E **81**, 041402 (2010).
[15] B. Schmittmann and R. K. P. Zia, *Phase Transition and Critical Phenomena*, 17th ed. (Academic, New York, 1995).
[16] B. J. van Wees, H. van Houten, C. W. J. Beenakker, J. G. Williamson, L. P. Kouwenhoven, D. van der Marel, and C. T. Foxon, Phys. Rev. Lett. **60**, 848 (1988).
[17] M. Dreher, F. Pauly, J. Heurich, J. C. Cuevas, E. Scheer, and P. Nielaba, Phys. Rev. B **72**, 075435 (2005).
[18] E. Scheer, N. Agrait, J. C. Cuevas, A. L. Yeyati, B. Ludoph, A. Martin-Rodero, G. R. Bollinger, J. M. van Ruitenbeek, and C. Urbina, Nature (London) **394**, 154 (1998).
[19] R. Haghgooie and P. S. Doyle, Phys. Rev. E **70**, 061408

(2004).
[20] A. Ricci, P. Nielaba, S. Sengupta, and K. Binder, Phys. Rev. E **74**, 010404 (2006).
[21] G. Piacente and F. M. Peeters, Phys. Rev. B **72**, 205208 (2005).
[22] E. B. Sirota, H. D. Ou-Yang, S. K. Sinha, P. M. Chaikin, J. D. Axe, and Y. Fujii, Phys. Rev. Lett. **62**, 1524 (1989).
[23] S. Hamaguchi, R. T. Farouki, and D. H. E. Dubin, Phys. Rev. E **56**, 4671 (1997).
[24] A. Yethiraj and A. van Blaaderen, Nature (London) **421**, 513 (2003).
[25] C. P. Royall, M. E. Leunissen, A.-P. Hynninen, M. Dijkstra, and A. van Blaaderen, J. Chem. Phys. **124**, 244706 (2006).
[26] S. Sengupta and A. K. Sood, Phys. Rev. A **44**, 1233 (1991).
[27] A. P. Hynninen and M. Dijkstra, J. Phys.: Condens. Matter **15**, S3557 (2003).
[28] R. Haghgooie and P. S. Doyle, Phys. Rev. E **72**, 011405 (2005).
[29] R. Haghgooie, C. Li, and P. S. Doyle, Langmuir **22**, 3601 (2006).
[30] J. T. G. Overbeek and E. J. W. Verway, *Theory of Stability of Lyophobic* (Elsevier, New York, 1948).
[31] B. V. Derjaguin, *Theory of Stability of Colloids and Thin Films* (Consultants Bureau, New York, 1989).
[32] D. L. Ermak, J. Chem. Phys. **62**, 4189 (1975).
[33] P. J. Steinhardt, D. R. Nelson, and M. Ronchetti, Phys. Rev. B **28**, 784 (1983).
[34] N. W. Ashcroft and N. D. Mermin, *Solid State Physics* (Saunders College Publishing, Philadelphia, 1976).
[35] J.-P. Hansen and L. Verlet, Phys. Rev. **184**, 151 (1969).
[36] P. N. Pusey, W. van Megen, P. Bartlett, B. J. Ackerson, J. G. Rarity, and S. M. Underwood, Phys. Rev. Lett. **63**, 2753 (1989).
[37] S. Auer and D. Frenkel, Nature (London) **409**, 1020 (2001).
[38] P. B. Bolhuis, D. Frenkel, S. Mau, and D. Huse, Nature (London) **388**, 235 (1997).
[39] S. Pronk and D. Frenkel, J. Chem. Phys. **110**, 4589 (1999).
[40] B. Cichocki and R. B. Jones, Physica A **258**, 273 (1998).
[41] S. Bhattacharya, J. Blawzdziewicz, and E. Wajnryb, J. Fluid Mech. **541**, 263 (2005).
[42] R. B. Jones, J. Chem. Phys. **115**, 5319 (2001).